ORIGINAL PAPER



Robust control of an actively controlled drogue for autonomous aerial docking

Alexander Funke¹ · Vivian Lück² · Gertjan Glabeke³

Received: 16 March 2025 / Revised: 17 June 2025 / Accepted: 25 June 2025 © The Author(s) 2025

Abstract

Automating the aerial docking procedure of two aircraft using the probe-and-drogue method can enable fully autonomous docking maneuvers for various applications in the future. For this purpose, a simplified system model of an actively controlled drogue was derived by combining the aerodynamic forces of control surfaces and the drogue body through superposition. Wind tunnel tests and computational fluid dynamics simulations were conducted to identify the aerodynamic coefficients, which were then used for model-based controller design. Robust control strategies such as sliding mode control, super twisting control, and PID control, which served as a baseline, were implemented and tested in a comprehensive probe-and-drogue simulation under various external disturbances. A super twisting disturbance observer was added to enhance the controllers' performance. Furthermore, all tested control architectures were modified by adding incremental nonlinear dynamic inversion to reduce perturbation rejecting controller gains while preserving control performance. The derived system model and the implemented controllers were shown to be effective for this control problem. Specifically, the application of incremental nonlinear dynamic inversion can lead to reduced control input variation without compromising control performance.

 $\textbf{Keywords} \ \ \text{In-air capturing} \cdot \text{Automated aerial refueling} \cdot \text{Probe-and-drogue} \cdot \text{Unmanned aircraft systems} \ (UAS) \cdot \text{Incremental nonlinear dynamic inversion} \cdot \text{Sliding mode control}$

Abbreviations

ACD Actively controlled drogue

AoA Angle of attack CA Client aircraft

CFD Computational fluid dynamics

CS Control surface
IAC In-air capturing
IAE Integral absolute error

INDI Incremental nonlinear dynamic inversion

NDI Nonlinear dynamic inversion

SMC Sliding mode control STA Super twisting algorithm

Alexander Funke
Alexander.Funke@dlr.de

Gertjan Glabeke Gertjan.Glabeke@vki.ac.be

Published online: 15 July 2025

- Institute of Flight Systems, German Aerospace Center (DLR), 38106 Brunswick, Germany
- Technische Universität Braunschweig, 38106 Brunswick, Germany
- ³ von Karman Institute for Fluid Dynamics (VKI), 1640 Rhode-St-Genèse, Belgium

STC Super twisting control

STDO Super twisting disturbance observer

TA Tanker aircraft/tow aircraft

UA Unmanned aircraft

Coordinate frame indices

 \square_a Aerodynamic frame

 \square_b Body frame

 \square_n Local frame (local tangent plane)

 \mathbf{R}_a^b Rotation matrix $(a \to b)$

1 Introduction

Aerial docking of two aircraft has numerous practical applications. The most common being aerial refueling, where a tanker aircraft (TA) is either pulling a drogue on a refueling hose in the so called probe-and-drogue system or transfers fuel through a boom attached to it (flying boom method) [1]. Depending on the atmospheric conditions, probe-and-drogue refueling can become a challenging task for the pilots of the client aircraft (CA). Active stabilizing systems of the drogue can reduce the effects of wind gusts and aerodynamic disturbances during docking [1–3]. This method can also be



adopted for unmanned aircraft (UA) [4], where an actively controlled drogue (ACD) can address issues of low docking efficiency and high error rate in autonomous aerial refueling missions [5].

The use of UA in both civil and military sectors has gained substantial growth over the past decade due to low purchasing cost, high availability and versatility, and the recent advances in technology. For example, in the "Gremlins" program initiated by the Defense Advanced Research Projects Agency (DARPA), a swarm of UA can serve as an alternative for fighter aircraft. For reasons of cost efficiency, they are recoverable by larger host aircraft, similarly to the probe-and-drogue method [6]. In the civil sector, on the other hand, aerial docking can be used to retrieve reusable rocket booster stages in the so-called 'in-air capturing' method (IAC) in order to reduce operational costs of orbital launch services [7, 8]. The tanker aircraft takes on the role of a tow aircraft and, instead of refueling the CA, the client is coupled to the ACD after docking and towed back to the launch site.

The concept of a refueling drogue with active control surfaces was first presented in the 70s with the goal to alleviate engagement difficulties during the docking maneuver [9]. In [2], drogue canopy manipulation is used to manipulate the relative position of the drogue. The flight mechanics are derived based on wind tunnel tests. A linear-quadratic regulator (LQR) strategy to dampen angular rates and accelerations is presented and evaluated in simulation. A similar approach is taken in [5], where canopy manipulation is used in conjunction with fuzzy control to cope with model uncertainty and external wind disturbances. The closed-loop setup is tested in a wind tunnel experiment. In [3], control surfaces mounted to the body of the ACD are used to manipulate the air flow around the drogue. A PI controller is used to dampen acceleration. Wind tunnel tests are carried out for system identification and closed-loop evaluation. To identify an accurate system model based on a superposition hypothesis, a computational fluid dynamics (CFD) simulation is used in [10] with a similar drogue design. In [11], cascaded PID controllers are subsequently implemented for pose control and evaluated in closed-loop simulation. The authors of [12] derive a model and implement a disturbance rejecting control strategy for the full cable-drogue-UA assembly after successful docking.

Control design of the ACD needs to take care of atmospheric disturbances and changing boundary conditions to extend the operating range and successfully stabilize and control the drogue in challenging environments. In addition to wind and gusts, the commanded velocity of the aerial refueling maneuver varies depending on the flight characteristics of the CA. Furthermore, depending on specific mission requirements, the targeted hose length might be adjusted, which would affect the magnitude and direction of the rope

force. In IAC specifically, changing the rope length during the mission plays an important role in the docking maneuver due to the lack of maneuverability of the CA. While parameters of PID controllers can be tuned according to particular tuning rules to gain robustness (e.g. [13]), there exist several other approaches to cope with external disturbances and uncertainties of the system model.

In sliding mode control (SMC), a nonlinear switching gain is introduced to counteract disturbances. It has been proven that correctly parameterized bounded perturbations of the system dynamics can be suppressed exceptionally well. While easily implemented, a high gain switching function can lead to actuator chattering. This in turn can be handled by introducing a boundary layer, effectively replacing the switching term with a saturation function at a small cost of tracking performance [14].

There exist many extensions for SMC: in higher order sliding mode control, the sliding condition is not only enforced on the sliding surface but also on its higher derivatives. A special form of this approach is the so called super twisting algorithm (STA) [15]. It has multiple benefits over conventional SMC, one of them is that it generates a continuous control signal without chattering [16]. Traditionally, SMC is combined with nonlinear dynamic inversion (NDI) to improve transient behavior. In NDI, the system equations are inverted, such that the overall system dynamics correspond to those of an integrator chain.

Incremental nonlinear dynamic inversion (INDI) is a sensor-based extension to NDI limiting the need of system knowledge to that of the input model based on incremental system dynamics. This partly leads to robustness against model inaccuracies. In the past decade, INDI mainly gained attention in the field of flight control [17, 18], being adapted to quadrotors [19] especially for use-cases in presence of disturbances [20] and actuator faults [21, 22]. Additionally, in [21] both of the previously mentioned methods are combined to reduce the required switching gains of SMC, while at the same time reducing the residual errors of INDI.

In this work, identification of the aerodynamic properties, modeling of the flight mechanics of an ACD, and implementation of multiple of the previously described robust control strategies for autonomous aerial docking based on the probe-and-drogue method are presented in the context of IAC. The overall objective is to contribute to improving the technological maturity of this technology.

The design of the drogue was first described in [23] and further explored in [24]. The current development state is shown in Fig. 1. The ACD is designed as a self-contained UA with its own autopilot, sensors, power system, data link telemetry and four independent control surfaces (CS). The sensors are internally fused to an accurate position and velocity estimate of the ACD, which are also transmitted to the CA via datalink. In our test setup, it is pulled by a thin



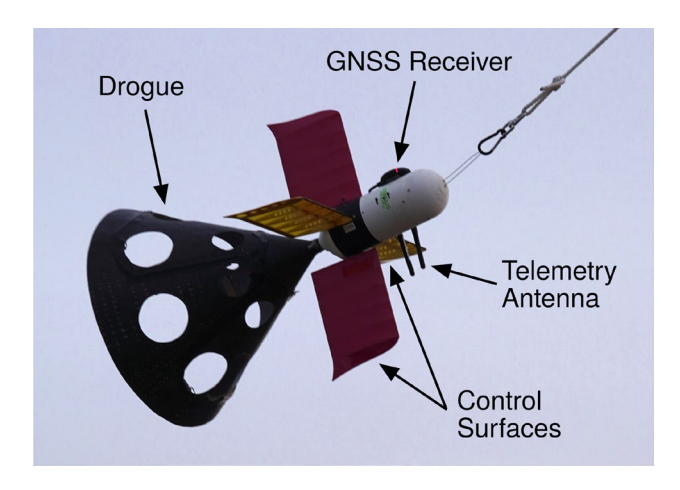


Fig. 1 Self-contained prototype of the ACD in flight

rope commonly used for tow operation in airplane model construction. First closed-loop results of the ACD were described in [25], which also includes flight test planning, sensor setup and the sensor fusion algorithm used for relative navigation.

A simplified model of the flight mechanics of the ACD is used for controller design to improve the command action of the closed loop. Two traditional cascaded PID control loops, extended with an input inversion term, serve as a baseline. Subsequently, INDI is implemented similarly to [19] with control allocation based on [26] and adapted to our use-case. Two sliding mode controllers, as described for first order in [14] and for second order in [16], are proposed. To lower the required switching gains and thus actuator chattering without affecting convergence of the sliding mode controller, a sliding mode disturbance observer based on the STA has been added to estimate the rope force for a fair comparison. Finally, a hybrid approach (incremental SMC) similar to [21] is tested to improve responsiveness and robustness, while preserving a stable flight of the ACD.

Carrying out flight tests with all of the proposed controllers is time and resource intensive. Thus, in this work, we first analyze the behavior of all methods in simulation in order to select a control architecture and parameter set for future flight testing. Our research has shown that all of the proposed controllers are suitable for this task. However, two controllers stand out by achieving lower control actions than their competitors while maintaining excellent control performance.

1.1 Main contribution

This work contributes to modelling of the flight mechanics and robust controller design of the ACD in a probeand-drogue system. While previous work mainly focused on compensating disturbances due to wake vortices or turbulence, we present and compare a control architecture of multiple robust model-based controllers to actively reposition the drogue relative to a fast moving CA under turbulence, model parameter uncertainties, varying rope length, sensor errors, and various delays. We evaluate the controllers based on their performance and feasibility in a comprehensive simulation.

2 Methods

This chapter is structured as follows: in Sect. 2.1, the aero-dynamic properties of the ACD are being identified in wind tunnel tests and CFD simulations. Then, in Sect. 2.2, the derived aerodynamic parameters are utilized to create a non-linear state space model, which is finally used to implement multiple robust controllers described in Sect. 2.3.

2.1 Aerodynamics

Wind tunnel tests were conducted to determine the force coefficients of the ACD prototype for various angles of attack (AoA) and CS deflections, covering a representative range of flight velocities (80–180 km/h). The results are utilized to construct high-fidelity aerodynamic tables, which are used in the simulation of the drogue. Additionally, they serve as basis for a simplified model of the flight mechanics described in Sect. 2.2, which is used for control synthesis in Sect. 2.3.

These tests took place in the closed test section of the von Karman Institute's (VKI) low-speed wind tunnel, designated L1-B, which is shown in Fig. 2b. The rectangular test section, measuring 2 m in height and 3 m in width, is equipped with a six-component platform balance. This balance, calibrated using OIML class F2 calibration weights, has a measurement chain uncertainty of 0.7% for loads and 2% for moments (full scale), and is integrated into the wind tunnel floor. The maximum free-stream wind velocity in the test section is 55 m/s, measured using a Prandtl-tube connected to an AMS5812 differential pressure sensor, which has a measurement chain uncertainty of ± 0.075 m/s. Under normal ambient meteorological conditions, this corresponds to approximately Mach 0.2. The turbulence intensity level, determined using hot wire anemometry, is 0.3% with a uniform inflow profile.

The ACD model is supported on the platform balance using a three-point arrangement: two main struts bear the full weight of the model, with the two horizontal control surfaces replaced by a rod, and one aft actuator allowing precise regulation of the AoA. The struts, made of aluminum Bosch profiles, are lightweight yet highly rigid against bending and are directly connected to the balance beneath the wind tunnel floor. To minimize wind exposure,



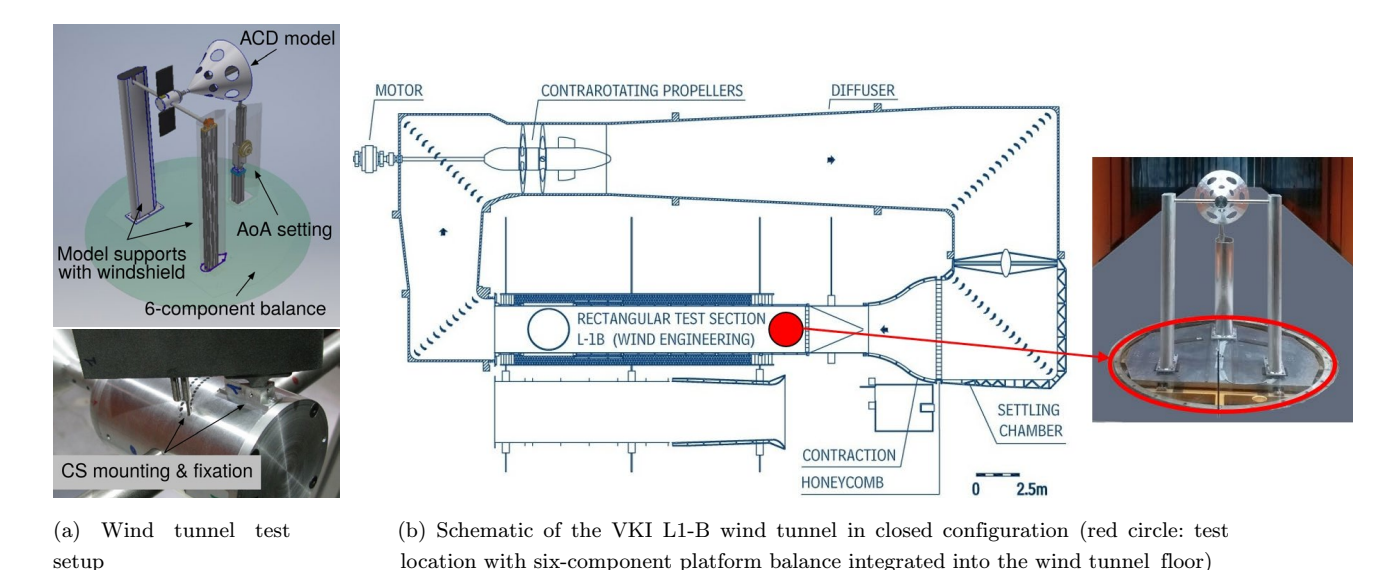


Fig. 2 Overview, setup and configuration of the ACD model in VKI's low speed wind tunnel

ellipse-sectioned aerodynamic fairings were constructed for these struts. Additionally, the control surfaces are fixed at two points on the model body, limiting their movement during tests at different AoA and control surface deflections, as shown in Fig. 2a.

The data obtained from wind tunnel tests were used to validate results obtained through CFD analysis, yielding a satisfactory validation. Subsequently, quantification of wind tunnel effects and correction of blockage due to wind tunnel walls, flow disturbances induced by model supports, and forces measured by non-shielded model supports were performed numerically. The CFD simulations (Fig. 3) were conducted using OpenFOAM, with a $k - \epsilon$ turbulence model, on the VKI in-house cluster "Frankenstein" and the Tier-1 supercomputer "Zenobe," operated by Cenaero in Belgium.

The computational domain is 11 m in length, with a distance of 2 m upstream from the model, and all other dimensions identical to the experimental setup as depicted in Fig. 3a. All solid surfaces are modeled as no-slip walls. At the inlet of the domain, the freestream velocity deduced from the Prandtl-tube measurements is imposed. In real flight conditions, all wind tunnel components (walls and supports) are removed. The boundary conditions remain identical except for the four wind tunnel walls, which are converted to slip walls to mimic freestream conditions.

The geometry is meshed using the snappyHexMesh utility of OpenFOAM. This utility automatically generates three-dimensional meshes comprising hexahedra and splithexahedra from triangulated surface geometries in stereolithography format (.stl). The mesh is refined iteratively to conform to the surface, with the resulting split-hex mesh then morphing to align with the surface. It is necessary to

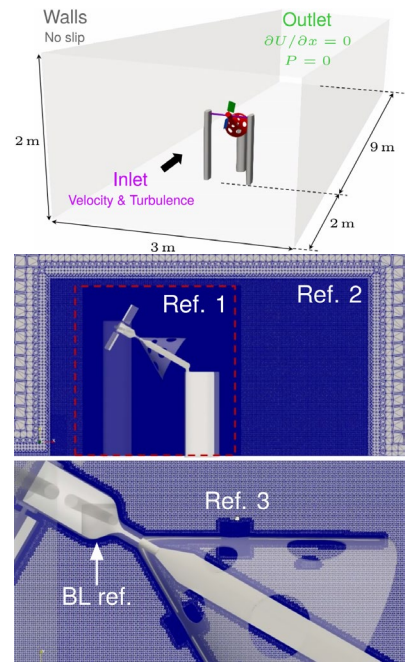
create several refinement zones in order to properly capture the flow gradients in the region of interest surrounding the ACD model as shown in Fig. 3a. Two additional refinement boxes (referred to as 'Ref. 1' and 'Ref. 2') are created around the model and its support structure, in addition to the extrusion volumes (referred to as 'Ref. 3') through each cone hole. These more confined flow passages can give rise to considerable acceleration and, consequently, necessitate the use of more refined meshes to prevent numerical divergence. Similarly, boundary edge grading ('BL ref.') is incorporated around all solid surfaces to ensure the accurate representation of viscous effects. Finally, edge refinements are employed to guarantee the precision of the geometry resulting from the surface morphing procedure.

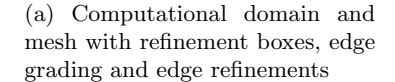
In Fig. 3b the flow visualization of the ACD wind tunnel test setup is depicted for large AoA and CS deflections. Under these conditions, flow separation can be observed at the edges. Additionally, the local flow behind the CS and the drag cone is substantially slowed down because of the high aerodynamic drag.

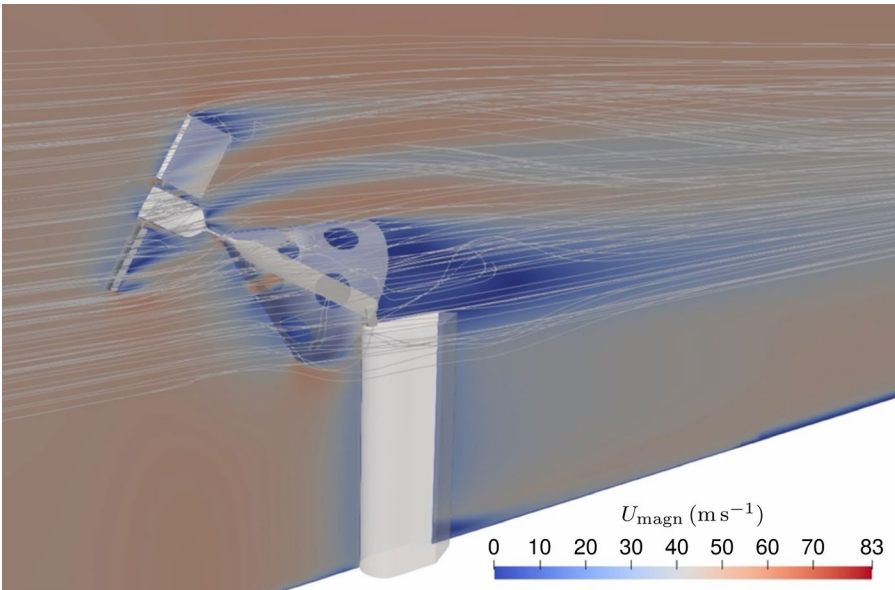
2.2 Modeling

The aerodynamic look-up tables derived from the wind tunnel tests and CFD simulations are used in our comprehensive probe-and-drogue simulation, which is implemented in MATLAB®/Simulink® and is originally based on [27]. The simulation contains several aerodynamically derived models, partly originating from wind tunnel and CFD analysis (ACD) and partly modeled with the vortex lattice method (TA and CA). The behavior of the individual models was verified in flight and driving tests and if necessary adjusted.









(b) Flow visualization from CFD simulation of the ACD model including the wind tunnel base for an AoA of 30°, asymmetric control surface deflection of $\eta_i=40^\circ$ and a free-stream wind speed of 180 km/h. The velocity contours in the vertical symmetry plane and the flow streamlines surrounding the ACD are displayed

Fig. 3 CFD simulation of the ACD including the assembly construction inside of the wind tunnel

Because of the low weight of the scaled-down tow rope, the rope dynamics were simplified to a single-link spring-damper system. Additionally, a contact model for the drogue based on elastic collision was implemented. The disturbances considered in this simulation are wind and turbulence, which is based on a pre-calculated von Kármán wind turbulence model, datalink delay and corruption, sensor errors, sensor processing delays, and model errors.

In the following section, modeling of a reduced statespace system model for control design is described. Furthermore, simple actuator models and dead-time compensation is presented.

2.2.1 Flight mechanics

Modeling of the flight mechanics of the ACD is based on the superposition of the rope and gravitational forces as well as lift and drag forces of the four CS and the drag cone. In the data obtained from wind tunnel tests, it was observed that this approach is only valid for relatively small AoA and CS deflections ($< \sim 10^{\circ}$). One reason is that in some cases, the ACD's body shadows one of the CS, leading to decreased control authority. Similarly, large CS deflections can also change the aerodynamic flow

surrounding the drogue, which in turn affects the local AoA and sideslip angle of the drag cone. These nonlinear coupling effects are neglected in the model derivation described below. Additionally, to simplify the model equations, we assume no wind and use small-angle approximation for vector rotations relating to the aerodynamic frame.

The separated and corrected look-up tables derived from the wind tunnel tests are depicted in Fig. 4a . Given the linear approximation for the lift coefficient in attached flow conditions $C_l \approx C_{l\alpha} \, \alpha$ with $|\alpha| < \alpha_{\rm crit}$, the lift force is defined as

$$F_L(\alpha) = \frac{1}{2} \rho v_x^2 \cdot A \cdot C_{l\alpha} \alpha, \tag{1}$$

where the term $\frac{1}{2} \rho v^2$ corresponds to the dynamic pressure p_{dyn} (in pa), specifically ρ is the air density (kg/m³) and v is the velocity of the fluid (m/s). Note that for model simplification, the velocity v_x in body frame is used here. For the CS, the reference surface area A (in m²) equals $A_\eta = 0.015$ m² and in case of the drag cone, $A_C \approx 0.061$ m² is assumed. The parameter $C_{l\alpha}$ describes the gradient of the lift coefficient, α is the AoA (rad), and specifically $\alpha_{\rm crit}$ is the critical AoA at which the flow separates from the surface. Due to the symmetry of the CS and the cone, the lift coefficient vanishes when the AoA is approaching zero.



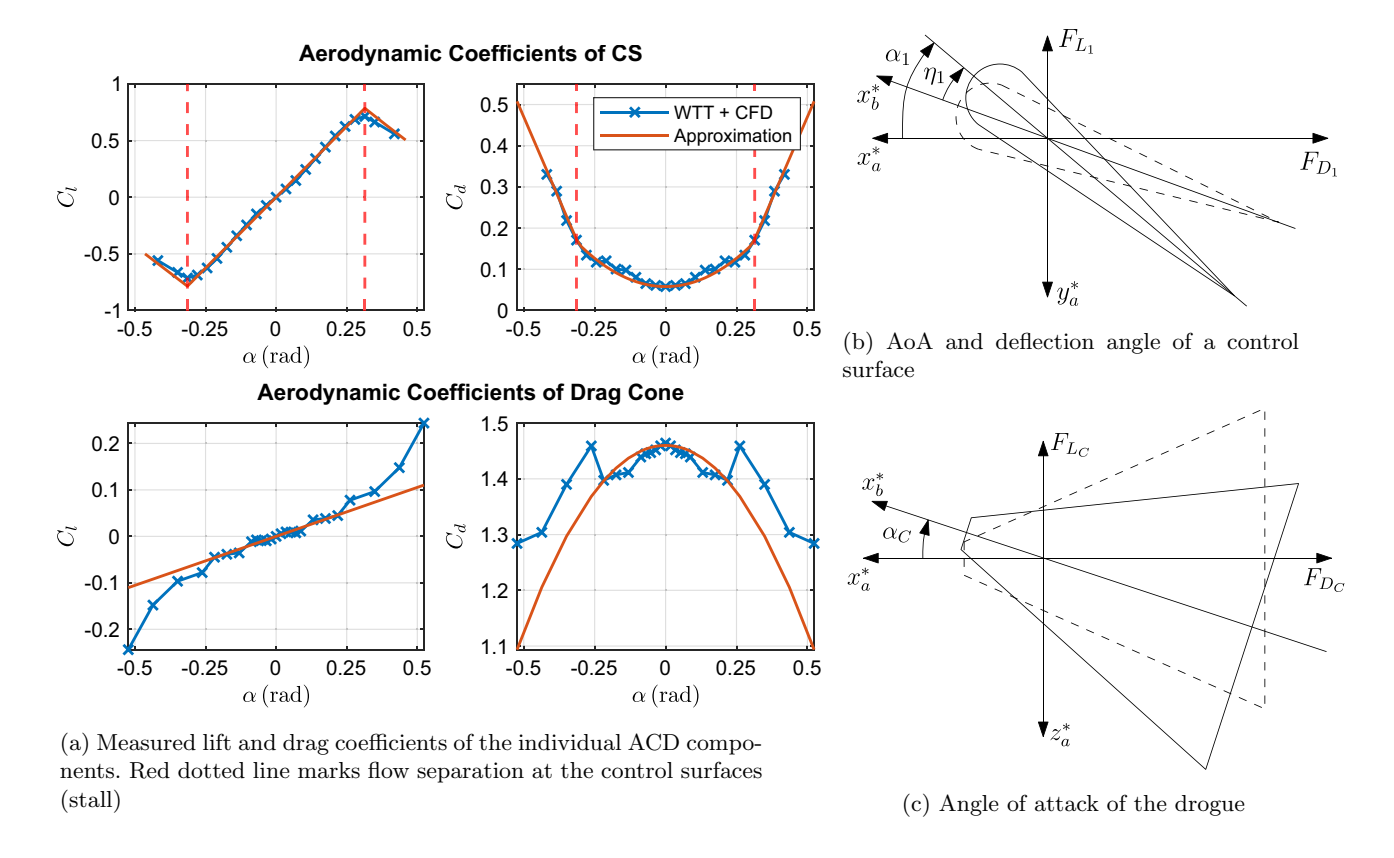


Fig. 4 Aerodynamic coefficients and forces of the ACD from wind tunnel tests and CFD simulations

To account for airflow separation at high AoA, we add the parameter C_{l0} to the approximation of the lift coefficient in equation (1) to receive the modified lift force

$$F_L^{\star}(\alpha) = \frac{1}{2} \rho v_x^2 \cdot A \cdot \left(C_{l\alpha} \alpha + C_{l0} \operatorname{sgn}(\alpha) \right), \tag{2}$$

which is valid for $|\alpha| > \alpha_{\rm crit}$. The drag coefficient of the CS is approximated as $C_d \approx (C_{d0} + C_{d1} \, \alpha + C_{d2} \, \alpha^2)$. Therefore, the drag force is given by

$$F_D(\alpha) = \frac{1}{2} \rho v_x^2 \cdot A_{\eta} \cdot \left(C_{d0} + C_{d1} \alpha + C_{d2} \alpha^2 \right)$$
 (3)

and for the drag cone the drag force is calculated as

$$F_{D_C}(\alpha, \beta) = \frac{1}{2} \rho v_x^2 \cdot A_C \cdot \left(C_{d0} + C_{d2} \cdot \left(\alpha^2 + \beta^2 \right) \right). \tag{4}$$

A table of aerodynamic coefficients of the single ACD components is shown in Table 1. For now, the parameters C_{l0} and C_{d1} that are accounting for the nonlinear stalling behavior are neglected in controller design but later will be applied to the system model used in the disturbance observer.

Figure 5 shows the geometry of the ACD and most of the acting forces on the body. Table 2 is supplementing the figure with the dimensions of the ACD prototype used in our experiments. The position vectors from the center of gravity to the force application points of the CS are defined as

$$\boldsymbol{r}_{1} = \begin{bmatrix} r_{Rud} \\ 0 \\ -r_{Ail} \end{bmatrix}, \ \boldsymbol{r}_{2} = \begin{bmatrix} r_{Ele} \\ -r_{Ail} \\ 0 \end{bmatrix}, \ \boldsymbol{r}_{3} = \begin{bmatrix} r_{Rud} \\ 0 \\ r_{Ail} \end{bmatrix}, \ \boldsymbol{r}_{4} = \begin{bmatrix} r_{Ele} \\ r_{Ail} \\ 0 \end{bmatrix}. \tag{5}$$

The local velocity of the individual CS is then given by

Table 1 Approximated aerodynamic coefficients of the ACD components in attached and separated flow conditions

Flow	Attac	ched				Separated				
Aerodyn. coeff.	$\overline{C_{l0}}$	$C_{l\alpha}$	C_{d0}	C_{d1}	C_{d2}	$\overline{C_{l0}}$	$C_{l\alpha}$	C_{d0}	C_{d1}	C_{d2}
Control surface	_	2.5	0.06	0.0	1.1	1.33	-1.8	-0.33	1.6	0.0
Drogue	-	0.21	1.46	_	-1.34	0.0	0.21	1.46	-	-1.34

The parameters C_{l0} and C_{d0} are dimensionless, $C_{l\alpha}$ and C_{d1} are in 1/rad, and C_{d2} is in 1/rad²



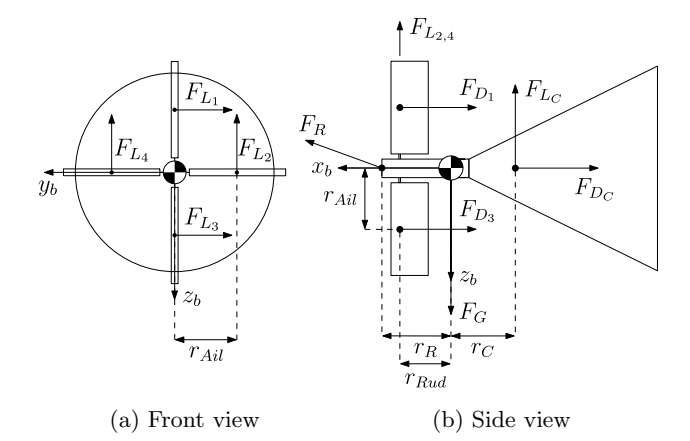


Fig. 5 Technical drawing of the ACD with forces acting on the body (depicted for $x_b = x_a$ and $z_b = -z_n$)

Table 2 Lever arm dimensions of the ACD

	r_{Ail}	r_{Ele}	r_{Rud}	r_C	r_R
Distance (m)	0.095	0.1	0.1	0.2	0.15

$$\mathbf{v}_i = \mathbf{v} + \boldsymbol{\omega} \times \mathbf{r}_i, \tag{6}$$

where ω is the angular velocity of the ACD (rad/s). The AoA of each CS is composed of the local inflow and the CS deflection η_i (in rad), as shown in Fig. 4b for the first CS. Given the AoA of the CS under small-angle approximation

$$\alpha_1 = \frac{v_{1_y}}{v_x} + \eta_1, \ \alpha_2 = \frac{v_{2_z}}{v_x} - \eta_2, \ \alpha_3 = \frac{v_{3_y}}{v_x} - \eta_3, \ \alpha_4 = \frac{v_{4_z}}{v_x} + \eta_4,$$
(7)

the forces of the CS are acting in the opposite direction of the CS deflection. Inserting (7) into (1) and (3), the force vector of each CS is then defined as

$$\boldsymbol{F}_{i=\{1,3\}} = \begin{bmatrix} -F_D(\alpha_i) \\ -F_L(\alpha_i) \\ 0 \end{bmatrix}, \ \boldsymbol{F}_{i=\{2,4\}} = \begin{bmatrix} -F_D(\alpha_i) \\ 0 \\ -F_L(\alpha_i) \end{bmatrix}. \tag{8}$$

As depicted in Fig. 4c, the AoA and sideslip angle of the cone

$$\alpha_C = \frac{v_z + \omega_y r_C}{v_x}, \ \beta_C = \frac{v_y - \omega_z r_C}{v_x}$$
 (9)

are calculated similarly. Inserting (9) into (1) and (4), the force vector of the drag cone is given by

$$\boldsymbol{F}_{C} = \begin{bmatrix} -F_{D_{C}}(\alpha_{C}, \beta_{C}) \\ -F_{L}(\beta_{C}) \\ -F_{L}(\alpha_{C}) \end{bmatrix}. \tag{10}$$

Assuming a high ratio of longitudinal to lateral velocity and thus again applying small-angle approximation, the AoA and the sideslip angle of the ACD are

$$\alpha = \frac{v_z}{v_x}, \ \beta = \frac{v_y}{v_x}.\tag{11}$$

Under the assumption of no wind, the rotation matrix

$$\mathbf{R}_{a}^{b} = \begin{bmatrix} 1 & -\beta & -\alpha \\ \beta & 1 & 0 \\ \alpha & 0 & 1 \end{bmatrix} \tag{12}$$

rotates the aerodynamic force vectors given in Eqs. (8) and (10) from the aerodynamic into the body frame. The rotation matrix

$$\mathbf{R}_{b}^{n} = \begin{bmatrix} c\psi \ c\theta \ c\psi \ s\theta \ s\phi - s\psi \ c\phi \ c\psi \ s\theta \ c\phi + s\psi \ s\phi \\ s\psi \ c\theta \ s\psi \ s\theta \ s\phi + c\psi \ c\phi \ s\psi \ s\theta \ c\phi - c\psi \ s\phi \\ -s\phi \qquad c\theta \ s\phi \qquad c\theta \ c\phi \end{bmatrix}$$
(13)

rotates from body into local frame with the Euler angles $\varphi = (\phi \ \theta \ \psi)$ (in rad) and the matrix

$$\mathbf{R}_{b}^{\varphi} = \begin{bmatrix} 1 & \sin(\phi)\tan(\theta) & \cos(\phi)\tan(\theta) \\ 0 & \cos(\phi) & -\sin(\phi) \\ 0 & \sin(\phi)\cos^{-1}(\theta) & \cos(\phi)\cos^{-1}(\theta) \end{bmatrix}$$
(14)

describes the relation between angular velocities of the ACD and derivatives of the Euler angles. The system model is then defined by the kinematic

$$\dot{p} = v \tag{15}$$

$$\dot{\boldsymbol{\varphi}} = \boldsymbol{R}_{b}^{\varphi} \,\boldsymbol{\omega} \tag{16}$$

and the dynamic equations

$$m\dot{\mathbf{v}} = \mathbf{R}_a^b \cdot \left(\mathbf{F}_C + \sum_{i=1}^4 \mathbf{F}_i\right) + \mathbf{F}_R + \mathbf{R}_b^{n^{\mathsf{T}}} \mathbf{F}_G$$
 (17)

$$\Theta \dot{\boldsymbol{\omega}} = -\boldsymbol{\omega} \times \boldsymbol{\Theta} \boldsymbol{\omega} + \boldsymbol{r}_{C} \times \boldsymbol{R}_{a}^{b} \boldsymbol{F}_{C} + \sum_{i=1}^{4} \left(\boldsymbol{r}_{i} \times \boldsymbol{R}_{a}^{b} \boldsymbol{F}_{i} \right) + \boldsymbol{r}_{R} \times \boldsymbol{F}_{R}$$

$$(18)$$

that result from the Newton-Euler equations and the equilibrium of forces and moments with the mass $m = 0.65 \,\mathrm{kg}$ and the inertia tensor of the ACD $\Theta = \mathrm{diag}(0.00477 \, 0.02022 \, 0.02023)\mathrm{kg} \,\mathrm{m}^2$. The force equilibrium is calculated by rotating and adding Eqs. (8) and (10), the unknown rope force F_R (in N), and the weight $F_G = m \cdot (0 \, 0 \, 9.81)^{\mathrm{T}} \,\mathrm{m/s^2}$.



2.2.2 Actuator dynamics and system delay

The actuators of the ACD are driven by simple RC servos, typically used in model aircraft. They contain a potentiometer to enable closed-loop control for the commanded servo position. We approximate the transient behavior of the closed-loop dynamics as a first-order lag element with the transfer function

$$G_{\text{PTI}}(s) = G_{\text{act}}(s) = \frac{1}{1 + Ts}.$$
 (19)

We use the discrete-time transfer function

$$G_{\text{act}}(z) = \left(1 - e^{-\frac{T_s}{T}}\right) \frac{z}{z - e^{-\frac{T_s}{T}}}$$
 (20)

with a sample time of $T_s = 0.01 \,\mathrm{s}$. The time constant $T = 0.0124 \,\mathrm{s}$ was obtained from lab experiments.

The position of the ACD in the formation of TA and CA $p_k = p_k^{\rm ACD} - p_k^{\rm CA}$ (in m) is measured relatively to the nosetip of the CA. Because of space limitations in the scaled prototype, the optical sensors are located within the nose of the CA and the measurement data will be transferred to the ACD via datalink. Detailed information of the sensor setup used can be found in [25]. Sensor processing and transmission of the estimated states back to the ACD incorporate system delay T_d (in s), which can partly be compensated by using the past velocity $v_{k-i}^{\rm ACD}$ (in m/s) and acceleration $a_{k-i}^{\rm ACD}$ (in m/s²) measurements of the ACD's flight controller. Assuming the acceleration of the CA $a_k^{\rm CA}$ is near-constant in the time period of the last T_d seconds, we compensate the data link delay by using the FIR-filter

$$p_{k} = p_{k-n} - T_{d} v_{k-n}^{CA} - \frac{T_{d}^{2}}{2} a_{k-n}^{CA} + \sum_{i=0}^{n} z^{-i} \left(T_{s} v_{k}^{ACD} + \frac{T_{s}^{2}}{2} a_{k}^{ACD} \right)$$
(21)

with the time step lag $n = \lfloor T_d/T_s \rfloor$. By regularly syncing the timestamps of the flight controllers, we can estimate the actual time delay of the data link during the flight test. The observed delay typically lies in the range of 50 ms up to 100 ms.

2.3 Control synthesis

To ensure robustness against uncertainties such as external perturbations like wind and gusts as well as model inaccuracies like the simplifying assumptions made above, we compare three different control methods that are known for their robust properties. The goal is to design a robust controller which takes the relative position of the ACD in relation to

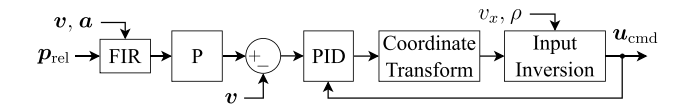


Fig. 6 Block diagram of cascaded P/PID controller for position control with input inversion

Table 3 PID controller parameters

	Inner-lo	Outer-loop		
	P	I	D	P
p_y, p_z	40	270	0.12	4
ϕ	12	2	0.1	2.5

the nose-tip of the CA and the roll angle as controlled variables $\mathbf{x} = (p_y \ p_z \ \phi)^T$ and outputs the actuator deflections of the four control surfaces.

2.3.1 PID control

One of the most commonly used control techniques is PID control. It is very easy to implement, does not necessarily require system knowledge and can be tuned based on well established recipes. The derivative part of the PID controller counteracts external disturbances, while the integrator is eliminating steady-state error, leading to robustness against process variations.

In our setup, a cascaded PID controller (in parallel form) is serving as a baseline for comparison of the control performance to decouple the disturbances, mainly affecting the velocity, from the controlled variables. The inner control loop is thus handling the velocity error. The I- and D-part of the control law are counteracting wind and wind gusts as well as the rope force. For the outer loop that is used for position control, a simple P controller has proven to be sufficient, thereby reducing the parameter-set.

An anti-wind-up strategy (clamping) was implemented in the PID controller to limit integrator wind-up when the CS are saturated e.g. due to large lateral rope forces. Furthermore, we have added roll compensation based on the rotation matrix (13) to ensure that position control is independent from the roll angle of the ACD. Additionally, input inversion is added, essentially by rearranging Eq. (1) for $\alpha = \eta_i$, to incorporate the nonlinear relation between velocity and the lift forces of the CS. These additions result in the controller becoming independent of the roll angle and the airspeed so that the docking maneuver can be conducted in multiple different scenarios.

In Fig. 6 the block diagram for relative position control is illustrated. Control of the roll angle is handled equivalently without the need for coordinate transformation. Table 3



shows the control parameters used in our experiments. Parameter tuning was conducted by first starting off with a parameter set for the inner control loop based on the Ziegler–Nichols method and subsequently modifying the gains while observing actuator variation. The same procedure was then repeated for the outer loop.

2.3.2 Dynamic inversion

Traditionally, nonlinear dynamic inversion (NDI) is used to invert nonlinear system dynamics. This is usually done to linearize the plant, decouple system equations or to improve the transient response. To apply NDI, an accurate model of the actual system dynamics is required. This can become quite challenging for complex systems and might also require additional state observation.

To overcome the problem of model dependency, incremental nonlinear dynamic inversion (INDI) was introduced as a sensor-based approach. Initially, INDI was deduced based on the assumption that, when observing a small time increment, the influence of the state dependent system dynamics is negligibly small in contrast to the input fraction. This assumption is referred to as the *time scale separation principle* [28]. To hold the assumption, it is required that the sample time of INDI is sufficiently small.

For this procedure, the system equation is first linearized with a Taylor series expansion. By canceling the term referring to the state dependent dynamics and solving for the input u, we receive

$$\boldsymbol{u}_{\text{cmd}} = \boldsymbol{u}_0 + \boldsymbol{B}^{-1} \underbrace{(\boldsymbol{v} - \dot{\boldsymbol{x}}_0)}_{\text{-Av}}, \tag{22}$$

where $\mathbf{v} = (a_y \ a_z \ \dot{\omega}_x)^{\mathsf{T}}$ refers to the virtual control input, \mathbf{u}_0 is the estimated actuator position based on the transfer function (19) and $\dot{\mathbf{x}}_0$ refers to the measured acceleration. The Jacobian \mathbf{B} is calculated by linearizing Eqs. (17), (18). Because the control objective only relates to the lateral position and the roll angle, we use the 2nd and 3rd dimension of the force and the 1st dimension of the moment equations to derive the input matrix

$$\boldsymbol{B} = -\frac{1}{2}\rho \, v_x^2 \cdot A_{\eta} \cdot \begin{bmatrix} \boldsymbol{B}_F \\ \boldsymbol{B}_T \end{bmatrix},\tag{23}$$

which is composed of the submatrix

$$\boldsymbol{B}_{F} = m^{-1} \cdot \left(\begin{bmatrix} C_{l\alpha} & 0 & C_{l\alpha} & 0 \\ 0 & C_{l\alpha} & 0 & C_{l\alpha} \end{bmatrix} + 2 C_{d2} \begin{bmatrix} \beta \\ \alpha \end{bmatrix} \begin{bmatrix} \alpha_{1} & \alpha_{2} & \alpha_{3} & \alpha_{4} \end{bmatrix} \right)$$

$$(24)$$

for the lateral force component and the submatrix

$$\boldsymbol{B}_{T} = \frac{r_{Ail}}{\Theta_{-}} \cdot \left(C_{l\alpha} + 2 C_{d2} \left[\beta \alpha_{1} \quad \alpha \alpha_{2} \quad \beta \alpha_{3} \quad \alpha \alpha_{4} \right] \right)$$
 (25)

for the torque component. For clarification, in slip-free conditions the input matrix reduces to

$$\mathbf{B} = -\frac{1}{2}\rho \, v_{x}^{2} \cdot A_{\eta} \cdot C_{l\alpha}$$

$$\cdot \begin{bmatrix} m^{-1} & 0 & m^{-1} & 0\\ 0 & m^{-1} & 0 & m^{-1}\\ r_{Ail} \, \Theta_{xx}^{-1} & r_{Ail} \, \Theta_{xx}^{-1} & r_{Ail} \, \Theta_{xx}^{-1} & r_{Ail} \, \Theta_{xx}^{-1} \end{bmatrix}.$$
(26)

Because of the high noise of the measured acceleration and the derivative of the measured angular velocity, when using micro-electromechanical systems (MEMS) based sensors, low-pass filtering is required to dampen high frequency oscillations [19]. Here, a Butterworth-filter of second order is used with a cut-off frequency of $\omega_c=30\,\mathrm{rad/s}$. In Fig. 7, the block diagram of INDI is shown. It should be noted that the low pass filter also needs to be added to the actuator command feedback, so that the phase delays of the virtual control input and the estimated actuator position are matched.

If the number of available actuators is not equal to the number of controlled variables and thus the input matrix is not square, the Moore–Penrose inverse can be used to invert the input matrix. In our case, the ACD is overactuated with four CS and three controlled variables p_x , p_y and ϕ . To additionally take actuator constraints into account, we solve the weighted least squares problem

$$\underset{\Delta u}{\operatorname{arg \, min}} \| \boldsymbol{W}_{\boldsymbol{u}} (\boldsymbol{u}_0 + \Delta \boldsymbol{u}) \|^2 + \gamma \| \boldsymbol{W}_{\boldsymbol{v}} (\boldsymbol{B} (\boldsymbol{u}_0 + \Delta \boldsymbol{u}) - \Delta \boldsymbol{v}) \|^2$$
s.t. $\boldsymbol{u}_{\min} \leq \boldsymbol{u}_0 + \Delta \boldsymbol{u} \leq \boldsymbol{u}_{\max}$ (27)

based on the active set method for control allocation, as described in [26]. The weighting parameters γ , W_u and W_v , which equally distribute the actuator commands to each CS and normalizing the roll angle offset to the position error, are given in Table 4.

Recently, a new generalized formulation of INDI not relying on the time-scale separation principle was

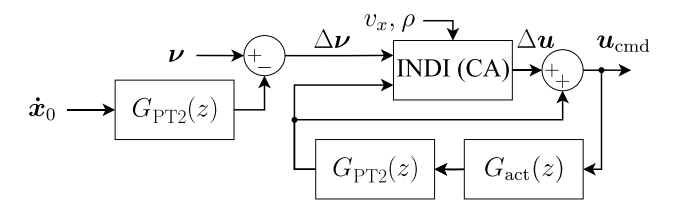


Fig. 7 Block diagram of INDI with low-pass filters

Table 4 INDI control allocation weighting parameters

	γ	W_u	$\overline{W_{ u}}$
Weights	100	diag(1 1 1 1)	diag(1 1 10)

introduced in [28], where stability and robustness properties were analyzed in depth.

2.3.3 Variable structure control

In variable structure control, a nonlinear control law, usually in the form of a switching mechanism, is used to handle model uncertainties and external perturbations. Sliding mode control (SMC) is one of those control methods to deal with nonlinear and uncertain systems. This is achieved by first transforming a complex *n*th-order system with a notational simplification into a more manageable 1st-order system and then applying the nonlinear switching law to the latter. This, in principle, enables 'perfect' performance to be achieved despite arbitrary parameter inaccuracies [14].

Consider the input-affine 2nd-order system

$$\dot{x}_1 = x_2
\dot{x}_2 = f(x) + g(x) \cdot u,$$
(28)

which follows the same structure as the previously derived system model (15)-(18). The state vector $\mathbf{x} = (\mathbf{x}_1 \ \mathbf{x}_2)^{\mathsf{T}}$ is composed of the previously defined controlled variable $\mathbf{x}_1 = (p_y \ p_z \ \phi)^{\mathsf{T}}$ as well as the lateral and angular velocity $\mathbf{x}_2 = (v_y \ v_z \ \omega_x)^{\mathsf{T}}$, the derivative of the controlled variable. The second derivative corresponds to the acceleration and angular acceleration $\dot{\mathbf{x}}_2 = (a_y \ a_z \ \dot{\omega}_x)^{\mathsf{T}}$. The system function $f(\mathbf{x})$ can be derived from Eqs. (17) and (18) omitting the rope force while the input matrix $g(\mathbf{x})$ is given by Eq. (26).

To reduce the relative degree of the previously defined 2nd-order system, we define the sliding surface with the parameter $\lambda \in \mathbb{R}^+$

$$s_1 = x_2 + \lambda x_1,\tag{29}$$

which corresponds to the 1st-order transformation mentioned above. By choosing the Lyapunov candidate

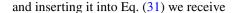
$$V(s_1) = \frac{1}{2}s_1^2, \quad \dot{V}(s_1) = s_1 \dot{s}_1$$
 (30)

and by inserting (28) and (29) into (30), we get

$$\dot{V}(s_1) = s_1 \cdot (f(x) + g(x) \cdot u + \lambda x_2) \stackrel{!}{<} 0.$$
 (31)

By then selecting the control input

$$u_{\text{cmd}} = \frac{-k \cdot \text{sign}(s_1) - \lambda x_2 - f(x)}{g(x)}$$
(32)



$$\dot{\mathbf{V}}(\mathbf{s}_1) = -k \cdot \operatorname{sign}(\mathbf{s}_1) \, \mathbf{s}_1 < 0, \tag{33}$$

which always holds for a positive switching gain $k \in \mathbb{R}^+$. Here, $g^{-1}(x)$ is calculated as Moore–Penrose inverse because the ACD is overactuated for the given control problem with its four CS.

It can be shown that this proof also holds for perturbed systems if the perturbation is bounded and the switching gain k is carefully chosen based on the maximum perturbation (see [14]). In this case, the perturbation corresponds to the model simplifications applied and the omitted rope force in Eq. (28).

A commonly described downside of sliding mode control is chattering of the actuators. To reduce chattering, the signum function can be replaced by a saturation function with the additional smoothing parameter $\kappa \in \mathbb{R}^+$ leading to the control input

$$\boldsymbol{u}_{\text{cmd}} = \frac{-k \cdot \text{sat}(\kappa \, \boldsymbol{s}_1) - \lambda \, \boldsymbol{x}_2 - f(\boldsymbol{x})}{g(\boldsymbol{x})}.$$
 (34)

This will reduce chattering, but also in turn softens the robustness guarantees and will affect tracking performance [14].

Notice that the control law also contains a plant inversion term $-f(x)g^{-1}(x)$, which can be substituted by INDI described above. This can be done to lower the switching gains in presence of model uncertainties and thus reducing chattering in the process [21].

As an alternative approach a higher order sliding mode controller can be used, which will apply the switching term to the derivative of the sliding surface and by that reducing chattering in the actuator output. A special form of 2nd-order SMC can be achieved with the so called super twisting algorithm (STA)

$$\dot{s}_1 = -k_1 \cdot \pm \sqrt{|s_1|} + s_2 \tag{35}$$

$$\dot{\mathbf{s}}_2 = -k_2 \cdot \operatorname{sign}(\mathbf{s}_1) \tag{36}$$

first mentioned in [15]. By selecting the parameters $k_1, k_2 \in \mathbb{R}^+$ carefully, robust stability with bounded perturbations in either or both of \dot{s}_1 and \dot{s}_2 is proven in [29]. This algorithm is applied to the control problem by choosing the control input

$$\boldsymbol{u}_{\rm cmd} = \frac{-k_1 \cdot \pm \sqrt{|s_1|} - \int_0^t k_2 \, \text{sign}(s_1) \, d\tau - \lambda x_2 - f(x)}{g(x)} \tag{37}$$

corresponding to the control law of SMC given in Eq. (32) (cf. [16]). This controller is referred to as super twisting controller (STC). To avoid integrator windup when the control surfaces are stalling, we added integrator saturation.



2.3.4 Disturbance observation

To lower the switching gains required for finite-time convergence of SMC and STC, model uncertainties like the rope force can be determined with a disturbance observer instead. By using the measured velocity $\mathbf{x} = \mathbf{v}$ and gravity adjusted acceleration $\dot{\mathbf{x}} = \mathbf{a}$ of the ACD, we estimate the rope force $\hat{\mathbf{F}}_R = m\hat{\mathbf{d}}$ by using a sliding mode disturbance observer based on the STA, the super twisting disturbance observer (STDO). Consider the system model

$$\dot{\hat{x}} = f(x) + g(x) \cdot u + \hat{d} \tag{38}$$

referring to the previously described flight dynamics model of the ACD in Eqs. (17), (28). For state observation, we approximate the control input as $\boldsymbol{u} = G_{\rm act}(s) \cdot \boldsymbol{u}_{\rm cmd}$ with $G_{\rm act}(s)$ from Eq. (19).

The measurement residuals

$$e = x - \hat{x} \tag{39}$$

$$\dot{e} = \dot{x} - \dot{\hat{x}} \tag{40}$$

are obtained by subtracting the estimated acceleration in Eq. (38) from the measurements. The estimated velocity \hat{x} can be calculated by integrating the estimated acceleration $\dot{\hat{x}}$. The sliding surface

$$s_1 = \dot{\boldsymbol{e}} + \lambda \, \boldsymbol{e} \tag{41}$$

is chosen to make use of acceleration and velocity measurements. By applying the STA and assuming the rope induced snap is upper bound by $|\ddot{\vec{a}}| < D$, we obtain

$$\dot{\hat{\boldsymbol{d}}} = -\lambda \, \dot{\boldsymbol{e}} - k_1 \cdot \pm \sqrt{|s_1|} + s_2$$

$$\dot{s}_2 = -k_2 \cdot \operatorname{sign}(s_1).$$
(42)

By integrating the estimated jerk \hat{d} , we finally receive the observed acceleration \hat{d} induced by the rope. The observer error converges to zero in finite time when choosing the gains as $k_1 = 1.5 \sqrt{D}$ and $k_2 = 1.1 D$ [16]. The upper bound of the snap can not directly be derived from technical aspects. However, in simulation and flight experiments, a value of $D = 250 \, \text{m/s}^4$ has been proven to be effective.

A simplified block diagram for relative position control of SMC with a STDO and NDI is shown in Fig. 8. The controller and observer parameters that were used in simulation are given in Table 5.

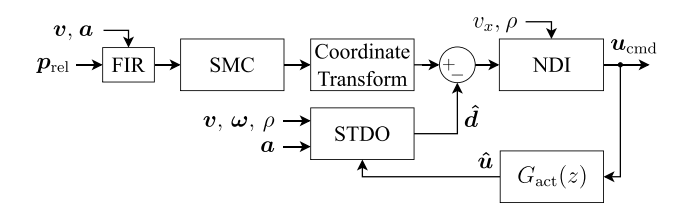


Fig. 8 Block diagram of SMC with STDO and NDI

3 Results

The following results were obtained in our scaled probeand-drogue simulation for the IAC scenario described in Sect. 2.2. The CA, in this case a reusable launch vehicle demonstrator, is gliding on a 10° downwards slope with a velocity of 160 km/h without engine power. The TA builds up the flight formation autonomously by setting down in front of the CA as described in [8] and keeping the distance to the CA constant. After formation build-up (at $t_{sim} = 20 \text{ s}$), the active control of the ACD is activated to reduce the relative position error and to keep the flight steady and stable in the presence of wind disturbance (gusts of $\pm 10 \,\mathrm{km/h}$). A winch is used to keep the distance to the CA constant, thereby changing the rope length in the process. In the beginning of the docking process, the rope length is quite short with 4 m. In the simulation it gets unwound to up to 12 m.

3.1 Disturbance observer

First, the performance of the STDO is evaluated. In Fig. 9, the simulated (F_R) and estimated (\hat{F}_R) rope forces are depicted for the closed-loop simulation.

After a short settling period in the beginning, the sliding variable has reached the switching manifold, following the simulated rope force. Note that due to the design of the observer based on simplified system equations, the observed disturbances are not limited to the rope force but also other model uncertainties present in Eq. (38). In normal operation, the rope accounts for the majority of the disturbance, but especially when one of the CS is close to stalling, the previously derived model is inaccurate, leading to larger observed lateral disturbances (e.g. at $t_{\text{sim}} = \{25 \text{ s}, 30 \text{ s}\}$). However, this effect is mostly beneficial for control accuracy as it corrects the error resulting from model inaccuracies in NDI.

3.2 Controller performance

To control the relative position of the ACD in relation to the nose-tip of the CA, six control architectures were implemented in our probe-and-drogue simulation: a baseline PID controller (cf. Fig. 6), a PID controller with INDI instead



Table 5 SMC, STC and STDO parameters

	λ	k	κ
SMC	5	40	1.6
	λ	k_1	k_2
STC STDO	5 2	35 23.7	100 275

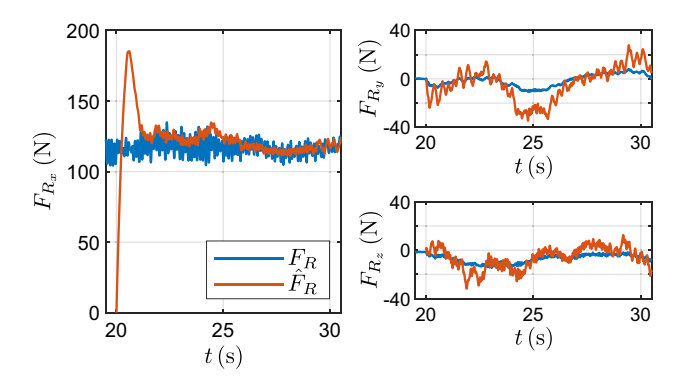


Fig. 9 Estimated vs simulated rope forces

Table 6 Adapted PID parameters

	Inner-1	oop		Outer-loop
	P	I D		P
$\overline{\text{PID}(p_y, p_z)}$	10	30	0.15	3.5

of input inversion (cf. Fig. 7), SMC with STDO and NDI (cf. Fig. 8), from now on referred to as 'SMC STDO,' SMC with INDI replacing NDI and omitting STDO referred to as 'SMC INDI,' STC with STDO and NDI, from now on referred to as 'STC STDO,' and STC with INDI replacing NDI and omitting STDO referred to as 'STC INDI'.

To reduce chattering, the switching gains of the sliding mode controllers with INDI were subsequently reduced as shown in Tables 6 and 7.

In Fig. 10, the results from closed-loop simulations are shown for all six control architectures. The relative position of the ACD in relation to the nose-tip is depicted in Fig. 10a for the control performance evaluation period from $t_{\rm sim} = 45 \, {\rm s}$ to $t_{\rm sim} = 75 \, {\rm s}$ visualized in Fig. 10b. Outside of this period the rope forces were to large to keep the ACD in front of the nose-tip. This is either because the rope length is too short or due to the TA not keeping the formation well

enough leading to a large lateral displacement. To make a fair comparison, the evaluation period was chosen such that no CS are saturated. Regarding the control objective, all controllers perform similarly well in this time interval (cf. Fig. 10a, d).

The actuator deflections are depicted in Fig. 10b. The overall shape of the curves of all actuator commands look similar. A closer look reveals that the controllers using INDI are driving the actuators faster and more often into their limits than their NDI counterpart. This is mainly because the simplified input model used in INDI is not containing an accurate model for CS stall to limit chattering. The incremental control law then leads to a quick accumulation of the actuator increments equally to a time-discrete integrator in PID controllers. SMC STDO has the smallest maximum actuator deflections overall, while PID INDI features significantly lower control input variation. This is also shown in Table 8.

The roll angle of the ACD during the active control period of the simulation is shown in Fig. 10c . In the evaluation time interval all controllers perform exceptionally well in keeping the roll angle close to zero. This can also be observed in Fig. 10d . However, outside of that period there exist some outliers mainly throughout short intervals when at least one of the CS is stalling. In INDI variants this effect is less prevalent and could be further reduced by limiting the maximum CS deflections to non-stalling conditions and tuning the control allocation weights accordingly. This, however, comes at the price of degrading performance of the position controller.

It can be observed that in SMC STDO the steady-state error of the roll angle is not vanishing. This happens because of model simplifications and missing integrating behavior in the rotational open-loop dynamics. Although small in magnitude, the torque induced by the rope is not accounted for by the STDO, thus leading to a constant offset. If problematic, this can be fixed by either implementing a torque

Table 7 Adapted SMC & STC parameters

	λ	k	К		λ	k_1	k_2
SMC	5	20	0.75	STC	5	10.6	55



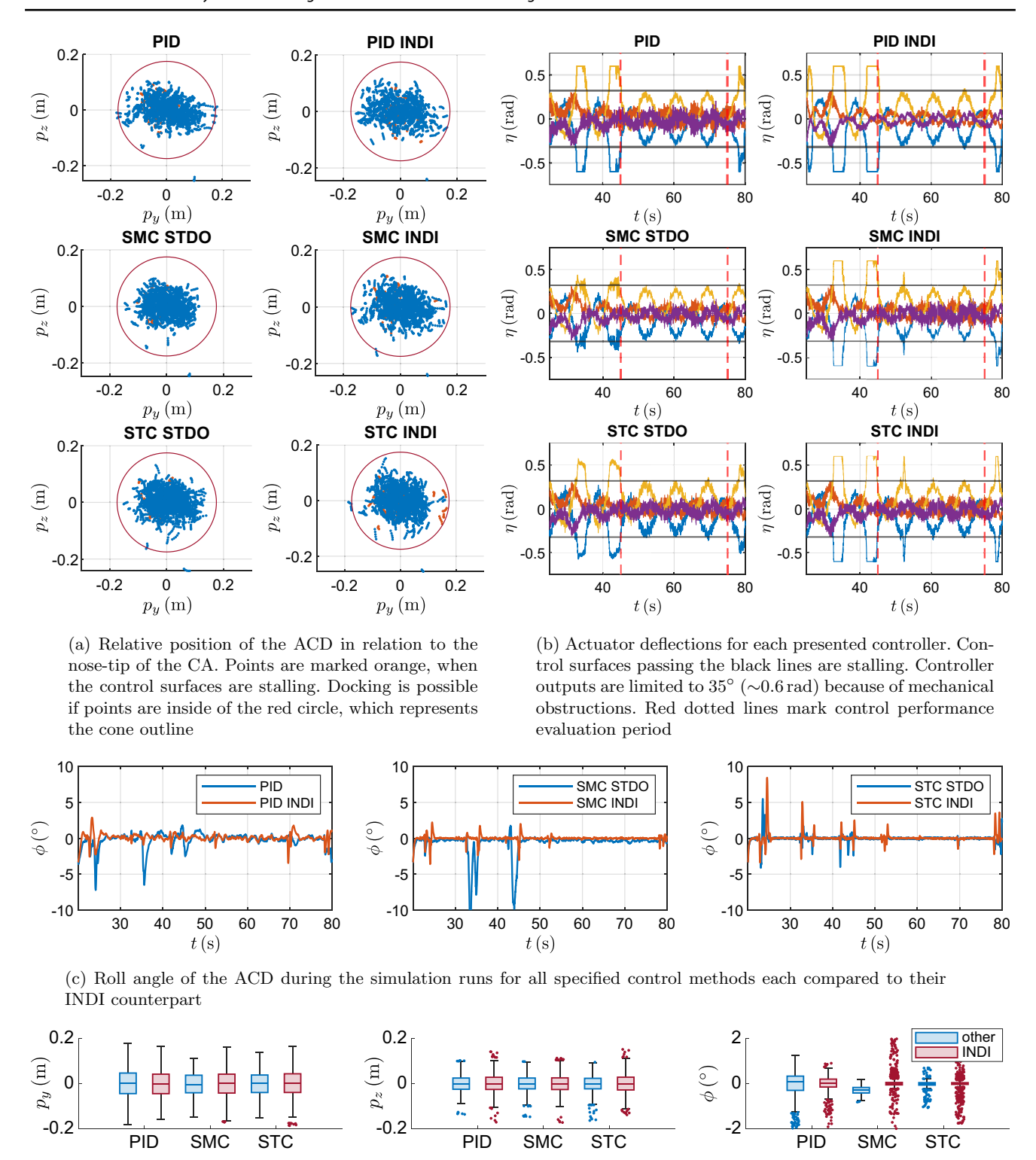


Fig. 10 Comparison of the controller performance of the previously presented methods

(d) Box plot of the relative position and roll angle errors of the ACD for each control architecture

disturbance observer or by using terminal SMC, an adaption of conventional SMC.

In Table 8, a comprehensive list of controller metrics is presented. The first section (I) is listing characteristics of a 1 m step-response of all six controllers. The transient



Table 8 Comparison of controller performance: the first section (I) shows the closed-loop transient response characteristics to a step input (cf. Fig. 11), the second and third sections display controller

metrics (II) and actuator properties (III) derived from a time fraction of the simulation runs (45–75 s)

			PID	PID INDI	SMC STDO	SMC INDI	STC STDO	STC INDI
(I)	Rise time (s)		0.48	0.37	0.42	0.52	0.35	0.45
	Settling time $(\pm 5\%)$) (s)		0.77	0.50	0.65	0.82	0.52	0.66
	Overshoot (%)		0.0	0.0	0.3	0.0	1.4	0.6
(II)	σ (Std. dev.)	y (m)	0.061	0.059	0.048	0.056	0.050	0.053
		z (m)	0.038	0.041	0.036	0.040	0.038	0.043
		ϕ (rad)	0.009	0.008	0.003	0.005	0.002	0.005
	IAE	y (m s)	1.496	1.438	1.209	1.393	1.239	1.292
		z (m s)	0.894	0.922	0.849	0.944	0.879	1.008
		ϕ (rad s)	0.196	0.156	0.162	0.056	0.037	0.056
	Docking success	(%)	97.97	98.83	99.70	98.70	99.63	98.37
(III)	Variance ($\times 10^3$)	$y (rad^2)$	15.67	16.49	14.76	16.20	15.88	18.68
		$z (\text{rad}^2)$	3.26	2.13	2.83	3.71	3.02	3.25
	Total variation	y (rad)	21.84	11.27	20.52	21.46	32.27	24.11
		z (rad)	59.60	11.41	49.27	46.48	45.25	31.39
	Max. deflection	y (rad)	0.45	0.34	0.31	0.47	0.36	0.60
		z (rad)	0.20	0.14	0.17	0.19	0.18	0.17

response of the closed-loop is shown in Fig. 11 below. Similar step-response metrics for all controllers can be observed (critical damping). PID INDI shows improved transient behavior in comparison to the conventional PID controller as expected. For both SMC STDO and STC STDO, INDI is not improving the transient response but instead reduces high-frequent steady-state oscillations considerably. With the additional gain k_1 in the control law of STC, the position feedback can be weighted independently of the velocity, which allows for more precise tuning in comparison to SMC. As a result, the target value of STC STDO is reached slightly faster when compared to SMC STDO.

In the second section (II), controller metrics for the evaluation period of the simulation presented above are displayed. The standard deviation of the control deviation highlights the dispersion of the control error. SMC STDO and STC STDO have a considerably lower standard deviation than the other controllers. PID and PID INDI perform comparably

worse in this metric. Additionally, the integral absolute error (IAE) of the PID controller describing the accumulated offset from the setpoint in the observed time period is worse in comparison to the other controllers. In this metric, SMC STDO performs best, with the exception of the roll angle, which has already been addressed above. The INDI versions of SMC and STC are performing slightly worse than the NDI counterpart. The difference between standard deviation and IAE metrics is that standard deviation only monitors dispersion, while IAE also accounts for stationary control deviation. The overall rate of docking success is very high (> 97.9 %). This metric describes the time ratio in which the probe of the CA fully lies inside of the cone outline of the ACD.

The last section (III) shows actuator performance throughout simulation. The variances of the control inputs are quite similar, as the ACD is exposed to the same disturbances in all simulation runs, resulting in comparable

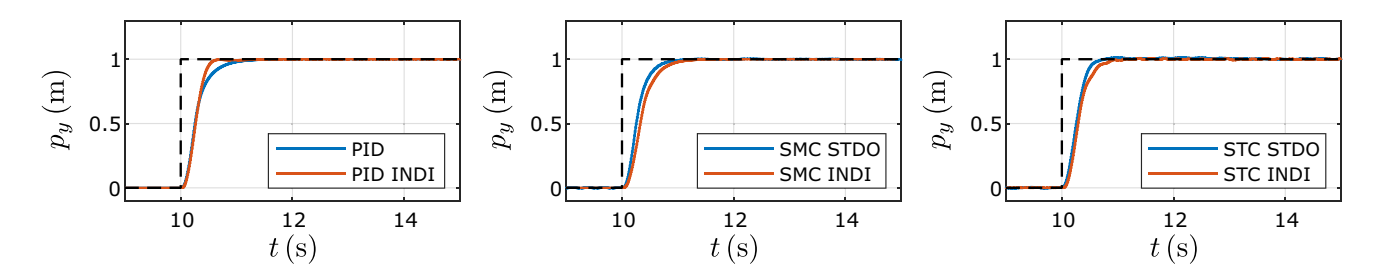


Fig. 11 Closed-loop step responses to a position jump of 1 m with a constant tow rope length of 20 m



CS deflections to keep the cone centered on the nose-tip. Total variation describes the total accumulated travel of the actuator. Despite reducing the controller gains of the INDI versions, the total variation of SMC INDI is not reduced as expected. This is most likely caused by the boundary layer of SMC being narrowed too much. Otherwise, the INDI modification has met its objective. This is especially the case for the PID controller, where the total variation is reduced by up to 80%.

To summarize, all controllers perform similarly well under changing external conditions and in the presence of disturbances. The remaining discrepancies can most likely be further reduced with additional controller tuning. During the evaluation period, SMC STDO demonstrates the best overall performance in this specific setup, while PID INDI stands out for its good control efficiency.

4 Discussion

As the simulations have shown, the derived simplified system model of the ACD is suited for model-based control design. Model errors can be accounted for by using robust control methods like SMC, INDI or disturbance observation. Combining these methods can lead to improved control performance while decreasing the necessary actuator deflections. Correctly tuned, PID controllers can result in almost equally good performance with only limited system knowledge. Nonetheless, performance can still be improved by combining PID with INDI.

It should be noted that the focus of the here presented work does not lie on generalized comparison of controller performance, but rather on the implementation details and their applicability to this control problem. However, in this setup, all controllers perform similarly well. INDI offers some advantages over traditional NDI, such as the reduction of controller gains without overly affecting performance and the inherent integrating behavior, which eliminates the need for a disturbance observer. All presented controllers are easy to implement and easy to tune. The total number of parameters necessary to adjust is limited to a handful, but increases slightly with the INDI and STDO extensions.

We have shown the applicability of the proposed controllers to actively reposition the drogue relative to the nose-tip of the CA in a scaled-down IAC mission under unknown disturbances, model uncertainties, and system delays. The results and control parameters determined in this study serve as a basis for future flight tests.



Fig. 12 Flight test of the ACD at the National Experimental Test Center for Unmanned Aircraft Systems in Cochstedt (Germany)

5 Conclusion

The presented work has demonstrated the feasibility of robust model-based controller design for the probe-and-drogue method with an actively controlled drogue by using a simplified system model derived from wind tunnel tests. The robust control methods implemented have shown to be effective in accounting for model errors and external disturbances, while achieving good control performance. Furthermore, the straightforward implementation and tuning of all controllers presented makes them suitable for practical applications. This research contributes to the development of advanced control strategies for the probeand-drogue method, which is essential for achieving autonomous docking maneuvers in future aerial refueling and in-air capturing missions.

5.1 Outlook

At the time of writing, the results of flight tests as shown in Fig. 12 are not yet available. It is planned to perform those tests in the future on a selection of the here presented controllers to supplement the results of this work with real-life flight test data.

Additionally, further investigations are required to analyze the closed-loop flight behavior of the ACD close to the nose-tip of the CA, where the so-called bow-wave effect causes the ACD to be pushed away from the probe shortly before docking. Finally, future work needs to address control performance in presence of actuator faults, since the drogue can quickly be damaged by unsuccessful docking attempts.

Acknowledgements We would like to thank Fabian Gücker from the Institute of Flight Guidance (TU Braunschweig) and Sophia Buckingham (formerly VKI) for their valuable support as well as Mark Spiller and Philipp Schitz from the Institute of Flight Systems (DLR) for their helpful feedback on variable structure control.



Author contributions The first draft of the manuscript was written by A. F. and all authors commented on previous versions of the manuscript. G. G. worked on aerodynamic characterization of the ACD. CFD simulations and wind tunnel tests were conducted at VKI. V. L. and A. F. worked on ACD model derivation and INDI implementation. A. F. complemented this design with PID, SMC, and observer synthesis as well as performance comparison. All authors read and approved the final manuscript.

Funding Open Access funding enabled and organized by Projekt DEAL. Parts of this work were performed under the Horizon 2020 project 'Formation flight for in-Air Launcher 1st stage Capturing demonstration' (FALCon) aimed at development and testing of the in-air capturing technology. FALCon was supported by the EU within work program 5.iiiLeadership in enabling and industrial technologies-Spacewith EC grant 821953. Further information on FALCon can be found atwww.falcon-iac.eu.

Data availability Simulation and CFD data generated within the research period are available on request from the corresponding author.

Declarations

Conflict of interest The authors have no competing interest to declare that are relevant to the content of this article.

Open Access This article is licensed under a Creative Commons Attribution 4.0 International License, which permits use, sharing, adaptation, distribution and reproduction in any medium or format, as long as you give appropriate credit to the original author(s) and the source, provide a link to the Creative Commons licence, and indicate if changes were made. The images or other third party material in this article are included in the article's Creative Commons licence, unless indicated otherwise in a credit line to the material. If material is not included in the article's Creative Commons licence and your intended use is not permitted by statutory regulation or exceeds the permitted use, you will need to obtain permission directly from the copyright holder. To view a copy of this licence, visit http://creativecommons.org/licenses/by/4.0/.

References

- Thomas, P.R., Bhandari, U., Bullock, S., Richardson, T.S., du Bois, J.L.: Advances in air to air refuelling. Prog. Aerosp. Sci. 71, 14–35 (2014). https://doi.org/10.1016/j.paerosci.2014.07. 001
- Williamson, W.R., Reed, E., Glenn, G.J., Stecko, S.M., Musgrave, J., Takacs, J.M.: Controllable drogue for automated aerial refueling. J. Aircr. 47(2), 515–527 (2010). https://doi.org/10.2514/1.44758
- 3. Kuk, T., Ro, K.: Design, test and evaluation of an actively stabilised drogue refuelling system. Aeronaut. J. 117(1197), 1103–1118 (2013). https://doi.org/10.1017/S00019240000087
- Nalepka, J., Hinchman, J.: Automated aerial refueling: extending the effectiveness of UAVs. In: AIAA Modeling and Simulation Technologies Conference and Exhibit (2005). https://doi.org/10.2514/6.2005-6005
- Meng, Z., Bai, J., Yan, B., Li, S.: An autonomous aerial refueling controllable drogue with adjustable strut angle: control and test. IEEE/ASME Trans. Mechatron. (2023). https://doi.org/10.1109/TMECH.2023.3339479

- Calhoun, P.: Darpa emerging technologies. Strateg. Stud. Q. 10(3), 91–113 (2016)
- Sippel, M., Klevanski, J., Kauffmann, J.: Innovative method for return to the launch site of reusable winged stages. In: 52nd International Astronautical Congress (2001)
- Stappert, S., Singh, S., Funke, A., Sippel, M.: Developing an innovative and high-performance method for recovering reusable launcher stages: the in-air capturing method. CEAS Space J. (2023). https://doi.org/10.1007/s12567-023-00512-0
- Ellsworth, J.A., Fox, W.R., Lovendahl, D.E., Moore, J.E.: Guided drogue flight test report. Technical Report E-23027 (ADA049164), Beech Aircraft Corporation, Defense Technical Information Center (1977). https://apps.dtic.mil/sti/citations/ ADA049164
- Singh, S., Bussler, L., Callsen, S., Stappert, S., Lopes, S., Buckingham, S.: A superposition approach to aerodynamic modelling of a capturing device used for in-air capturing of a reusable launch vehicle. In: 9th European Conference For Aeronautics And Space Science, EUCASS (2022). https://elib.dlr.de/ 187074/
- Singh, S., Simioana, M., Stappert, S., Sippel, M., Buckingham, S., Lopes, S., Kucukosman, Y.C.: Control design and analysis of a capturing device performing in-air capturing of a reusable launch vehicle. In: 9th European Conference For Aeronautics And Space Science, EUCASS (2022). https://elib.dlr.de/ 187073/
- Liu, Y., Wang, H., Fan, J., Wang, Y., Wu, J.: Trajectory stabilization control for aerial recovery of cable-drogue-uav assembly. Nonlinear Dyn. (2021). https://doi.org/10.1007/ s11071-021-06773-w
- Ge, M., Chiu, M.-S., Wang, Q.-G.: Robust PID controller design via LMI approach. J. Process Control 12(1), 3–13 (2002). https://doi.org/10.1016/S0959-1524(00)00057-3
- Slotine, J., Li, W.: Applied Nonlinear Control. Prentice-Hall, Englewood Cliffs (1991)
- Levant, A.: Sliding order and sliding accuracy in sliding mode control. Int. J. Control 58(6), 1247–1263 (1993). https://doi.org/ 10.1080/00207179308923053
- Chalanga, A., Kamal, S., Fridman, L.M., Bandyopadhyay, B., Moreno, J.A.: Implementation of super-twisting control: super-twisting and higher order sliding-mode observer-based approaches. IEEE Trans. Ind. Electron. 63(6), 3677-3685 (2016). https://doi.org/10.1109/TIE.2016.2523913
- Sieberling, S., Chu, Q.P., Mulder, J.A.: Robust flight control using incremental nonlinear dynamic inversion and angular acceleration prediction. J. Guid. Control. Dyn. 33(6), 1732– 1742 (2010). https://doi.org/10.2514/1.49978
- Grondman, F., Looye, G., Kuchar, R.O., Chu, Q.P., Kampen, E.-J.: Design and flight testing of incremental nonlinear dynamic inversion-based control laws for a passenger aircraft. In: AIAA Guidance, Navigation, and Control Conference (2018). https://doi.org/10.2514/6.2018-0385
- Smeur, E., Chu, Q., Croon, G.: Adaptive incremental nonlinear dynamic inversion for attitude control of micro air vehicles. J. Guid. Control. Dyn. 39(3), 450–461 (2016). https://doi.org/10. 2514/6.2016-1390
- Smeur, E., Croon, G., Chu, Q.: Cascaded incremental nonlinear dynamic inversion for MAV disturbance rejection. Control. Eng. Pract. (2018). https://doi.org/10.1016/j.conengprac.2018.01.003
- Wang, X., Kampen, E.J., Chu, Q., Lu, P.: Incremental sliding-mode fault-tolerant flight control. J. Guid. Control. Dyn. 42(2), 244–259 (2019). https://doi.org/10.2514/1.G003497
- Beyer, Y., Steen, M., Hecker, P.: Incremental passive fault-tolerant control for quadrotors subjected to complete rotor failures.
 J. Guid. Control. Dyn. 46(10), 2033–2042 (2023). https://doi. org/10.2514/1.G007475



- Cain, S., Krause, S., Binger, J.: First development steps of an actively controlled drogue. In: 2018 International Conference on Unmanned Aircraft Systems (ICUAS), pp. 660–669 (2018). https://doi.org/10.1109/ICUAS.2018.8453453
- Krause, S., Cain, S.: UAV pre-study for in-air-capturing maneuver. In: 2020 IEEE Aerospace Conference, pp. 1–14 (2020). https://doi.org/10.1109/AERO47225.2020.9172769
- Krause, S., Funke, A., Cain, S.: Overview of a planned subscale in-air capturing demonstration. In: 2024 IEEE Aerospace Conference, pp. 1–15 (2024). https://doi.org/10.1109/AERO58975. 2024.10521033
- Smeur, E.J.J., Höppener, D., Wagter, C.D.: Prioritized control allocation for quadrotors subject to saturation. In: International Micro Air Vehicle Conference and Flight Competition 2017, pp. 37–43 (2017). https://www.imavs.org/papers/2017/6.pdf
- 27. Dauer, J.C., Lorenz, S.: Modular simulation framework for unmanned aircraft systems. In: AIAA Modeling and Simulation

- Technologies (MST) Conference (2013). https://doi.org/10.2514/6.2013-4974
- Wang, X., Kampen, E.J., Chu, Q., Lu, P.: Stability analysis for incremental nonlinear dynamic inversion control. J. Guid. Control. Dyn. 42(5), 1116–1129 (2019). https://doi.org/10.2514/1. G003791
- Moreno, J.A., Osorio, M.: Strict Lyapunov functions for the super-twisting algorithm. IEEE Trans. Autom. Control 57(4), 1035–1040 (2012). https://doi.org/10.1109/TAC.2012.2186179

Publisher's Note Springer Nature remains neutral with regard to jurisdictional claims in published maps and institutional affiliations.

